IFASD 2015
International Forum on Aeroelasticity and Structural Dynamics
June 28 — July 02, 2015 ▲ Saint Petersburg, Russia

REDUCED-ORDER MODELLING AND FEEDBACK CONTROL OF INTEGRALLY ACTUATED MEMBRANE WINGS

Stefano Buoso and Rafael Palacios
Imperial College, London, SW7 2AZ, United Kingdom
r.palacios@imperial.ac.uk

Keywords: Fluid-Structure Interaction, Dielectric elastomers, Feedback control, Hyper-elastic, Low-Reynolds, Reduced-order modelling, System identification.

Abstract: This paper presents a numerical investigation on aerodynamic control of integrally-actuated membrane wings made of dielectric elastomers. They combine the advantages of membrane shape adaptability with the benefits of the simple, lightweight but high-authority control mechanism offered by integral actuation. For that purpose, high-fidelity numerical models have been developed to predict their performance. They include a fluid solver based on the direct numerical integration of the unsteady Navier-Stokes equations, an electromechanical constitutive material model and a non-linear three-dimensional membrane structural model. In addition, using the Eigensystem Realization Algorithm, it is obtained a very low order model description of the fully coupled aero-electromechanical system to aid the design of a simple PID control scheme for the feedback control of the wing. The resulting regulator is then implemented in the high-fidelity model and used for the mitigation of flow disturbances.

1 Introduction

Outdoor use of Micro Air Vehicles (MAVs) is limited by their low aerodynamic efficiencies and sensitivity to flow disturbances. In addition, flight instabilities arising from their small dimensions, require efficient control mechanisms. Natural fliers, such as small mammals and insects that are similar to MAVs for size and flying conditions, use wing compliance to efficiently compensate for flow disturbances and achieve high manoeuvrability and agility [1, 2]. Experimental investigations of membrane wing prototypes have in fact demonstrated that compliant wings can offer superior aerodynamic performance as compared to rigid wings, such as delayed stall, higher lift and increased stability [3, 4, 5, 6]. These aerodynamic advantages can also be used to mitigate the effect of flow disturbances in engineering vehicles, but the controllability of the highly-flexible MAVs remains as one of the main issues that needs to be solved for outdoor applications.

In bats, the skeleton stretching the membrane is an efficient control mechanism to tune in real time the aerodynamic characteristics of the wing. A similar concept can be reproduced in artificial membrane wings by embedding dielectric elastomers (DEs). They are composed of a thin polymeric layer sandwiched between two compliant electrodes. The

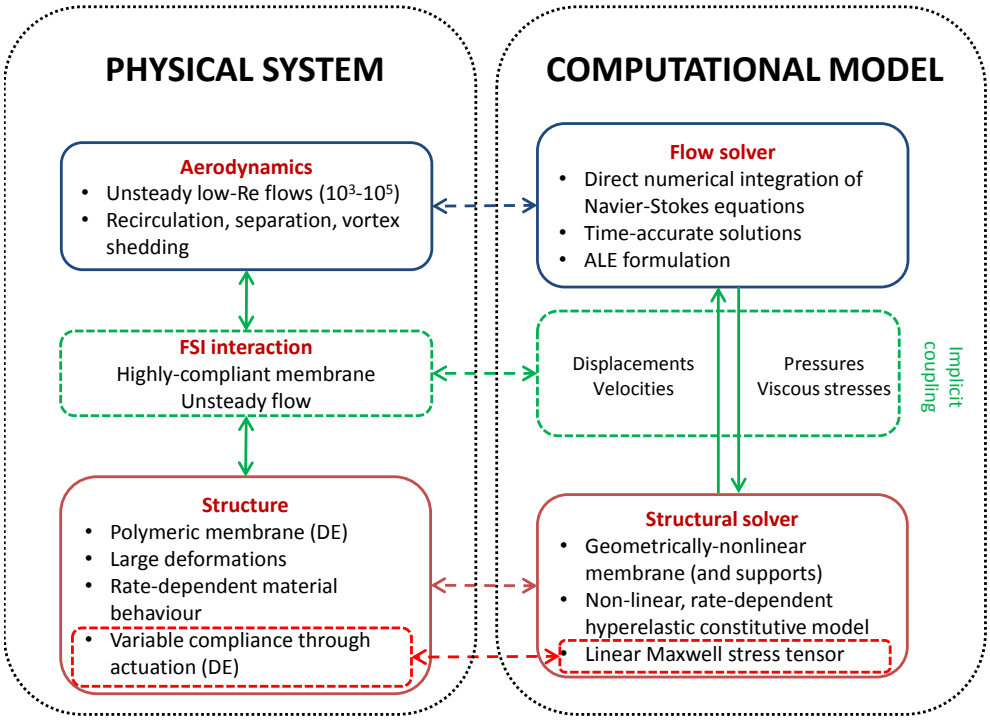

Figure 1: Definition of the aeroelastic problem of actuated membrane wings: physical system and the corresponding computational model used in this work.

application of a voltage through the thickness causes the compression of the material in that direction and its in-plane extension [7]. This defines a variation of the tension in the wing that can be used to tune its dynamic behaviour. Dielectric elastomers (DEs) show great promise since they combine the advantages of membrane wings with the benefits of a simple, lightweight control mechanism, and lead to an increase of specific performance and in the stability and controllability of the membrane wing. However, issues of material stability and the high-voltage requirements would need to be addressed before actual deployment as MAV wing skins [8].

Modelling and analysis of actuated membrane wings define an essentially multidisciplinary problem, covering aerodynamics, structural dynamics, material modelling and control aspects. The key characteristics of the resulting system are oulined in Fig.1. The highly unsteady flow dynamics brings a strong coupling with the compliant membrane, both in chordwise and spanwise directions [5, 9] – which may produce the aforementioned aerodynamic benefits. The structure, due to the high flexibility, is subjected to large displacements involving large strains and a rate dependent material constitutive behaviour. Arbos-Torrent et al. [6] have experimentally shown that mean camber and modes of membrane aerofoils are also strongly influenced by the size and shape of the leading- and trailing-edge supports which, in practice, can never be neglected. Finally, an electromechanical material model is required to characterise the actuation [7].

The modelling fidelity available for the aeroelastic analyhsis of passive membrane wings has improved together with the available computer power. 2D linear elastic structural model have been typically used, which have been coupled sucesively with potential-flow solvers [3], inviscid and viscous laminar solvers [10, 11] and implicit LES solvers [12]. For high-enough Reynolds numbers a major challenge is the modelling of the laminar-

turbulent transition under unsteady conditions. This was first addressed by Lian et al. [13] and Lian and Shyy [14], who developed an aeroelastic model including an hyper-elastic constitutive solver for the material and a e^N transition model for the fluid to investigate the lift produced by unsteady separation bubbles on membrane wings. Recently, a coupled high-fidelity model for actuated membrane wings that can consider all the fields involved and their interaction (see Fig. 1) has been proposed by Buoso and Palacios [15], who showed the effect of an open-loop control scheme on the aerodynamic performance of the wing.

From the experimental side, only Hays et al. [16] and Curet et al. [17] have to date tested the use of DEs to increase the performance of membrane wings. They have shown that both static and dynamic actuation can enhance the aerodynamic efficiency of the wing, measured as the mean lift-to-drag ratio.

Further to a previous work by the authors [15], this paper will investigate the potential gains in performance of dynamically actuated two dimensional membrane wings in low Reynolds number flows with a closed-loop feedback control system. Section 2 describes the high-fidelity aeroelastic model developed and introduces the model reduction technique based on the Eigensystem Realisation Algorithm (ERA). Section 3 presents numerical results of the performance of the wing in the steady and unsteady case. The reduced-order model (ROM) obtained with ERA is used for the design of a feedback control scheme for the wing which is then applied to the high-fidelity model to compensate for the flow-disturbances of the pressure field around the membrane.

2 Computational model

The structural is a geometrically non-linear solid finite-element discretization of the membrane, with non-linear constitutive relations for the DE and a linear electrostatic model for the Maxwell stresses. It is coupled, using an implicit time-marching algorithm with non-matching spatial discretisations, with a flow solver based on the direct numerical integration of the unsteady Navier-Stokes equations. The key features both models will be briefly described in Sections 2.1 to 2.3. For a detailed description the reader is referred to the previous work of the authors [15]. In Section 2.4 the model reduction technique based on the Eigensystem Realization Algorithm (ERA) is described.

2.1 Electromechanical Model

In the current approach, the thickness of the membrane is considered, allowing the definition of the electrostatic stress tensor in all three dimensions. The structural model will be solved using solid eight-nodes three-dimensional elements with translational degrees of freedom [18]. The large structural displacements requires a non-linear geometric structural description of the membrane and a non-linear constitutive model. The constitutive model for DE is developed in the finite-deformation framework [19, 20, 21] through the definition of a free energy function W

$$W = U(J) + \Phi_\infty(\bar{I}_1), \tag{1}$$

splitted into the contribution of a volumetric, U, and a deviatoric, Φ_∞, components, which depend on the deformation state of the solid. In particular, J is the determinant of the deformation gradient, $\boldsymbol{F}$, defined between the reference and the deformed configurations,

and $\bar{I}_1$ is the first invariant of the deviatoric part of the deformation gradient, defined as $\bar{\boldsymbol{F}} = \boldsymbol{F} J^{-2/3}$ (see Bonet [19] for details). The constitutive model assumes a nearly-incompressible isotropic material, with a voltage- and stretch-independent value of the dielectric constant. The selected deviatoric elastic constitutive law for the stress is the Gent model [22]

$$\Phi_\infty = -\frac{\mu J_m}{2} \log\left(1 - \frac{\bar{I}_1 - 3}{J_m}\right), \tag{2}$$

where μ and J_m are material coefficients that have to be determined experimentally. The model has been selected because it consists of two parameters of immediate physical meaning and it predicts the stiffening behaviour when the deformation approaches the value of the limiting stretch. The volumetric energy function is expressed by

$$U(J) = K(J-1)^2, \tag{3}$$

where K is the compressibility modulus of the material, that needs to be experimentally identified. Since in this work the material is assumed to be nearly-incompressible, high values of K have to be expected. The low amount of compressibility allowed from the inclusion of the volumetric stress component removes the numerical instabilities that would appear under a conservation of volume assumption. The constitutive model is then completed by adding the effect of the electrostatic stresses that are modelled with the Maxwell's stress tensor. Given an electric field vector $\boldsymbol{E}$, the stress tensor $\boldsymbol{\sigma}_e$ is defined as [7]

$$\boldsymbol{\sigma}_e = \epsilon \boldsymbol{E} \otimes \boldsymbol{E} - \frac{1}{2}\epsilon \left(\boldsymbol{E} \cdot \boldsymbol{E}\right) \boldsymbol{I}, \tag{4}$$

where ϵ is the material dielectric constant, $\boldsymbol{E}$ is the electric field vector in the deformed coordinate system and $\boldsymbol{I}$ is the unitary second order tensor. The material dielectric constant ϵ is usually expressed as $\epsilon = \epsilon_0 \epsilon_r$ where ϵ_0 is the vacuum dielectric constant and ϵ_r is the material relative dielectric constant. The total stress is finally obtained as $\boldsymbol{\sigma}$ [7]

$$\boldsymbol{\sigma} = \boldsymbol{\sigma}_m + \boldsymbol{\sigma}_e. \tag{5}$$

In this work, the VHB4905 acrylic dielectric elastomer is selected as material for the membrane wing and its constitutive model has been implemented in a user-subroutine in Abaqus [18]. The coefficients of the Gent material model used are μ= 20 kPa, J_m= 100 and K= 3.8×10^8 Pa, from a previous work from the authors [23], and the relative dielectric constant is $\epsilon_r = 2.7$ to match the experimental results of Refs [24, 25].

2.2 Fluid Model

The numerical model for the low-Reynolds flow is based on a finite-volume discretization of Navier-Stokes equations with second-order integration in space an time. The solution is based on the compressible-equations with a low-Mach preconditioner [26]. A coupled approach is used to solve the flow and energy equations, which requires more memory but offers better stability and velocity in the convergence. The boundary conditions for the single-membrane wing analysis include a constant pressure boundary condition at the outlet, and the specification of velocity magnitude and direction for all other far-field boundaries. In this work a 2D case is considered, hence periodic boundary conditions are imposed in the lateral surfaces of the domain. On the membrane walls a no-slip constrain is imposed.

In addition to the conventional studies on sensitivity to the grid-resolution and time step, which are described in Section 3, for each case considered the element size and time step have been compared with the characteristic viscous length and time scales, that is, $l_\nu = \nu/u_\nu$ and $t_\nu = l_\nu/u_\nu$, respectively, where ν is the kinematic viscosity of the fluid and u_ν is the friction velocity [27]. Assuming a volumetric average of the elements size, the characteristic length of the mesh elements is $l_{mesh} = \sqrt[3]{l_x l_y l_z}$ with l_x, l_y and l_z being the dimensions of the hexahedral cells. Appropriate spatial and temporal resolution of the smallest turbulence scales requires to have [28] $l^* = \frac{l_{mesh}}{l_\nu} \sim \mathcal{O}(1)$, $t^* = \frac{\Delta t}{t_\nu} \sim \mathcal{O}(1)$, where Δt is the time step of the implicit solvers. The fluid mesh selected for the simulations in this work, described in Sec. 3, is well within this range, with a value of l^* and t^* below 3 throughout the domain.

2.3 Fluid-Structure Coupling

The coupling of flow and structural solvers is carried out using a common interface that occupies the same spatial positions in both models. The mapping of the grid nodes between both meshed proceeds as follows [26]: First, neighbour nodes and elements are identified; next, the fluid solver uses the shape functions of the structural solver for the interpolation of the pressure and viscous forces and the definition of the equivalent set of nodal loads to be used in the finite-element solver; finally, the new nodal displacements and velocities from the FE solver are then passed to the fluid solver for the deformation of the mesh and the computation of the new flow field. The mesh deformation process moves the mesh nodes accordingly to a 3D linear interpolation law that is depending on their distance from the moving and fixed boundaries. The exchange of data between the solvers uses a bridge in the RAM memory [26].

An implicit coupling was found necessary, considering the strong interaction of the fluid and the membrane structure in this problem. When the relative difference in the norm of two consecutive field exchanges is below a defined tolerance (10^{-4} for the results in this work) convergence is established. The solution is initialised with a quasi-steady step, neglecting the inertia forces and velocities of the membrane, and is then restarted with a dynamic step to converge to the real solution.

2.4 Model Reduction: Eigensystem Realization Algorithm

As mentioned above, the high-fidelity is not directly usable for controller design and a reduced-order model description is needed. For that purpose, the fully coupled model is considered here as a single-input (voltage) / single-output (C_l) system. The model-reduction is based on the assumption that the fully-coupled electro-aeroelastic model can be described by a discrete linear system in the form

$$\boldsymbol{X}_{k+1} = \boldsymbol{A}\boldsymbol{X}_k + \boldsymbol{B}U_k, \tag{6a}$$

$$Y_{k+1} = \boldsymbol{C}\boldsymbol{X}_{k+1}, \tag{6b}$$

where $\boldsymbol{X}_k$ and $\boldsymbol{X}_{k+1}$ are the vectors of the identify system state variables at increments k and $k+1$, U and Y are the input and output of the system respectively, and $\boldsymbol{A}$, $\boldsymbol{B}$ and $\boldsymbol{C}$ are the matrices representing the evolution of the linear system.

From the reference configuration, which is identified by $\boldsymbol{X}_0 = \boldsymbol{0}$, the system is excited with an impulsive function. Under this conditions, the system outputs at any instant k can be expressed as $Y_k = \boldsymbol{C}\boldsymbol{A}^{k-1}\boldsymbol{B}$. The Henkel matrices $\boldsymbol{H}(0)$ and $\boldsymbol{H}(1)$ are defined as

$$\boldsymbol{H}(0) = \begin{bmatrix} Y_1 & Y_2 & \dots & Y_\gamma \\ Y_2 & Y_3 & \dots & Y_{\gamma+1} \\ \vdots & \vdots & \ddots & \vdots \\ Y_p & Y_{p+1} & \dots & Y_{\gamma+p-1} \end{bmatrix}, \qquad \boldsymbol{H}(1) = \begin{bmatrix} Y_2 & Y_3 & \dots & Y_{\gamma+1} \\ Y_3 & Y_4 & \dots & Y_{\gamma+2} \\ \vdots & \vdots & \ddots & \vdots \\ Y_{p+1} & Y_{p+2} & \dots & Y_{\gamma+p} \end{bmatrix}, \tag{7}$$

where p and γ are integers satisfying the relation $\gamma r \geq pm$ and r and m are the number of inputs and outputs of the system respectively. The Henkel matrix $\boldsymbol{H}(0)$, by means of the Singular Value Decomposition (SVD), is factorised in $\boldsymbol{H}(0) = \boldsymbol{R}\,\boldsymbol{\Sigma}\,\boldsymbol{S}^T$. The n non-zero eigenvalues of $\boldsymbol{\Sigma}$ (which are all non-negative [29]) are retained and $\boldsymbol{H}(0)$ can be written as $\boldsymbol{H}(0) = \boldsymbol{R}_n\,\boldsymbol{\Sigma}_n\,\boldsymbol{S}_n^T$, where $\boldsymbol{R}_n$ and $\boldsymbol{S}_n$ are obtained considering only the first n columns of $\boldsymbol{R}$ and $\boldsymbol{S}$ respectively. Writing $\boldsymbol{H}(0)$ in terms of the observability, $\mathcal{P}_p$, and controllability, $\mathcal{Q}_\gamma$, matrices it is obtained [29]

$$\boldsymbol{H}(0) = \left[\boldsymbol{R}_n\,\boldsymbol{\Sigma}_n^{\frac{1}{2}}\right]\left[\boldsymbol{\Sigma}_n^{\frac{1}{2}}\,\boldsymbol{S}_n^T\right] \cong \mathcal{P}_p\mathcal{Q}_\gamma \tag{8}$$

with $\mathcal{P}_p = \boldsymbol{R}_n\,\boldsymbol{\Sigma}_n^{\frac{1}{2}}$ and $\mathcal{Q}_\gamma = \boldsymbol{\Sigma}_n^{\frac{1}{2}}\,\boldsymbol{S}_n^T$. The matrices $\boldsymbol{A}$, $\boldsymbol{B}$ and $\boldsymbol{C}$ are then obtained as

$$\boldsymbol{A} = \boldsymbol{\Sigma}_n^{-\frac{1}{2}}\boldsymbol{R}_n^T\boldsymbol{H}(1)\boldsymbol{S}_n\boldsymbol{\Sigma}_n^{-\frac{1}{2}}, \tag{9a}$$

$$\boldsymbol{B} = \text{the first } r \text{ columns of } \mathcal{Q}_\gamma, \tag{9b}$$

$$\boldsymbol{C} = \text{the first } m \text{ rows of } \mathcal{P}_p. \tag{9c}$$

The reduced-order model identified in (6) is limited by the linear assumption and by the frequency range that is considered during the system identification, which is defined by the time window and time step selected. Still it can represent key relevant dynamics of the full system at a very low computational cost and will therefore be used in an iterative scheme for the design of the feedback control of the actuated membrane.

3 Numerical Results

The implementation of the electro-aeromechanical material model proposed in Sec.2 has been verified against the relevant literature in a previous work by the authros [15]. Here, it will be used to investigate the closed-loop operation of an integrally dynamically actuated 2D membrane wing made with of VHB4905 elastomer. The numerical simulations consider a Reynolds number Re = 2500, as done by Gordnier [12], with angle of attack $\alpha = 4°$ and $8°$. The DE membrane, which has an initial thickness $h = 0.05$ mm, is prestretched to 50% of its underformed length ($\lambda_p = 1.5$). The selected amount of deformation defines a relatively stiff case, but is representative of the values of stretch in common DEs applications.

In the aerodynamic model, the shape of the supports is neglected, and in the structural solver they are assumed to be rigid. The membrane is pinned at the lower side of the leading and trailing edge. The structural mesh is composed of 400 elements chordwise, and only one element in the thickness direction. Since a 2D problem is addressed, a single element is used in the spanwise direction as well. For each case considered, mesh-refinement and time-step sensitivity studies have been conducted in dynamic simulations on the fluid solver and the relative errors on the mean value of C_l and C_d as well as the

amplitudes and frequencies of the oscillations of their values were considered to establish convergence. The maximum relative error of those quantities was set to be below 2%. The resulting fluid domain extends for 100 chords in both directions and is meshed with around one million elements, which corresponds to 400 elementa along the membrane walls in the chordwise direction, 400 in the flow direction for the wake, and 400 elements in the radial direction from the chord. the smaller element at the membrane wall is 50 μm and the bigger elements, at the domain boundaries, are around twice the size of the membrane chord. The vertical coordinate of the points of the membrane presented, y^*, are non-dimensional quantities obtained with normalisation with the value of the maximum amplitude of the membrane with the same prestretch subjected to a uniform pressure equivalent to the free stream dynamic pressure $\Delta P_\infty = 0.5\rho V_\infty^2$. For temporal convergence, the maximum number of sub-iterations for each time-step is set to 10 and the limit relative tolerance for the monitored flow properties is set to 10^{-4}. Evolution histories of the structure and aerodynamic coefficients are presented as function of the non-dimensional time $t^* = tV_\infty/c$.

3.1 Passive configuration

The passive case for $\alpha = 4°$ is characterised by a steady-state solution with a maximum amplitude $y^* = 0.33$ at $x/c = 0.4$, where c is the chord length (red in Fig. 2). The lift coefficient is $C_l = 0.396$. In the second case, with $\alpha = 8°$, when it is observed the presence of self-excited oscillations due to the fluid-structure interaction, the averaged deformed shape has a maximum amplitude of $y^* = 0.85$ at $x/c = 0.31$ (blue line in Fig. 2). Consistently with experimental observations [6], the maximum-camber point is moving downstream because of the increased amount of separation. This generates a low pressure region towards the trailing edge that results in an increase of membrane displacements in that area. Since the membrane is relatively stiff, separation occurs at a low angle of attack. The time-averaged lift coefficient is $C_l = 0.83$, and its time evolution is shown in Fig 3a.

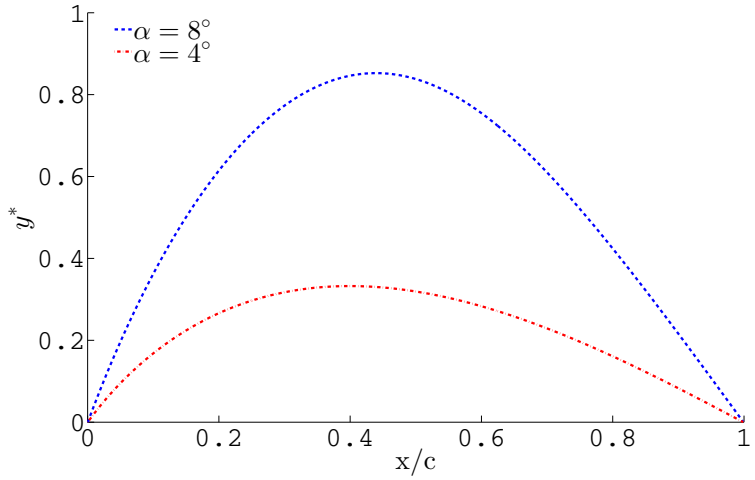

Figure 2: Mean deformed shapes for $\alpha = 4°$ and $8°$, Re $= 2500$, $\lambda_p = 1.5$.

A spectral analysis indicates the dominant contribution of a frequency content of 26 Hz, with secondary effects at 51 Hz, which is roughly twice the frequency. A POD analysis of the oscillations of the membrane over its mean value, Fig. 3b, shows a principal 1^{st}

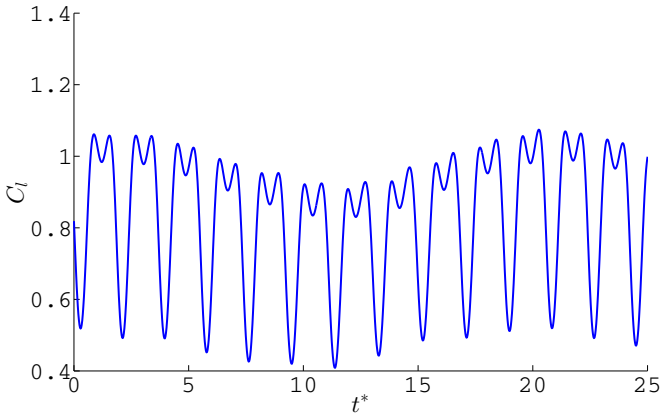

(a) C_l.

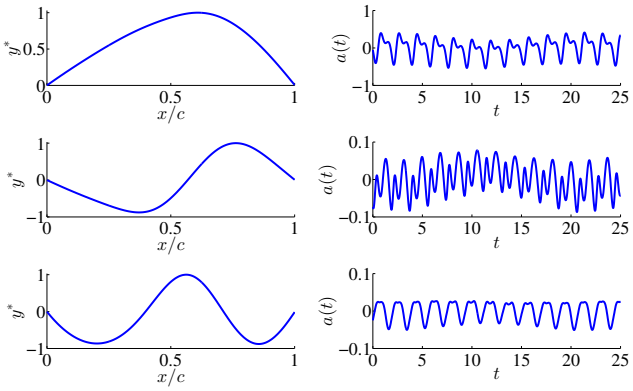

(b) POD analysis.

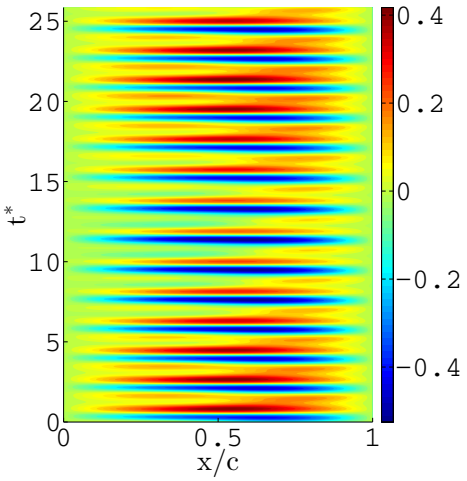

(c) y^* oscillations.

Figure 3: Passive membrane response at Re = 2500, $\lambda_p = 1.5$, $\alpha = 8°$.

vibrational mode, with the contribution of the 2^{nd} and 3^{rd} mode determining the chordwise displacement of the maximum amplitude point. The combination of the three determines the displacement history of Fig. 3c.

3.2 System Identification and Control Design

As discussed in the introduction, the main advantage of DE-based embedded actuation would be the rejection of flow disturbances and the achievement of "on-demand" aerodynamic performance. A closed loop-control system is then required to control in real time the actuation voltage of the DE. For the identification of the coupled system dynamics, the wing is excited with a pulse-signal and the simulation is run with a time range that goes from $t^* = 0$ to $t^* = 1.2$, in order to focus into the fast response of the wing, which is the one that is addressed by the control system. The time step is 10^{-4} s. Increasing the total simulation time would increase the contribution of the slow dynamics related to the convective time scale of the fluid, which are neglected in this work. The reduced-order system identified is a 10^{th} order dynamic SISO system. The comparison of the pulse-response of the high-fidelity system and the linear model identified is presented in Fig. 4, where the oscillations of the C_l over the mean value are plotted. The reduced-order model captures the main dynamic of the full-system for both frequency and amplitude of the oscillations, and showed convergence to the high-fidelity solution with the increase of

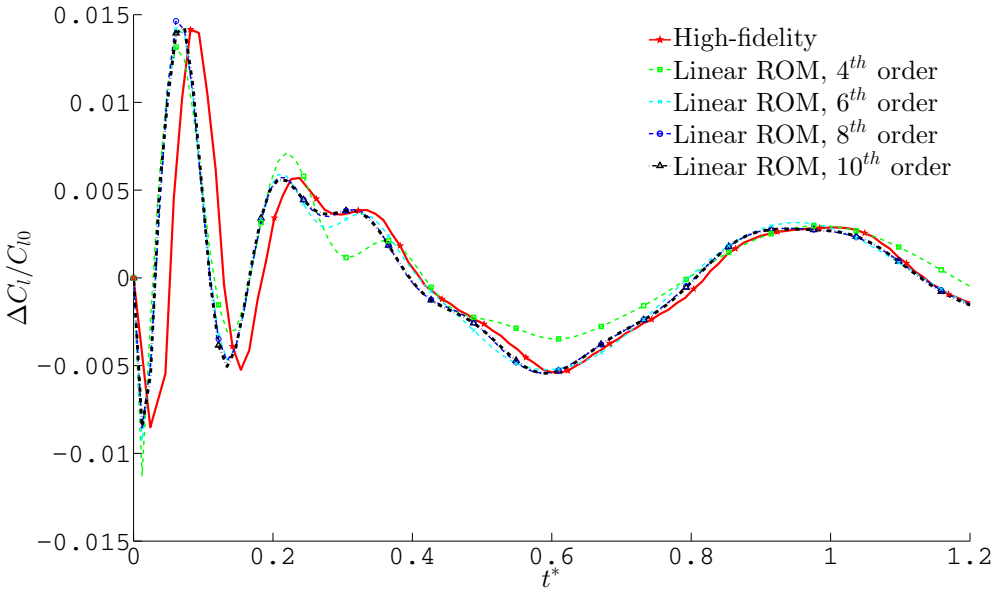

Figure 4: Comparison of the pulse-response of the high-fidelity model and linear system identified with ERA.

the order of the system.

The discrete dynamic system provides a good estimation of the fast dynamics of the actuated wing in the low Reynolds number flow considered and can be used as a tool for the preliminary design of a Proportional-Integral-Derivative (PID) controller for the wing. The controller is then defined as

$$V^2(t) = K_i \int_0^t e(\tau)d\tau + K_p e(t) + K_d \dot{e}(t) \tag{10}$$

where V is the applied voltage, K_i, K_p and K_d are the integral, proportional and derivative gains, and $e(t) = C_{l,ref} - C_l(t)$ is the instantaneous error between the reference lift coefficient for the control system, $C_{l,ref}$ and the lift coefficient of the system, C_l. The continuum form description of the controller can be conveniently discretised and coupled with the linear system identified. The SISO system defined does not include the possibility of defining pressure variations on the membrane, so the control system design is done considering the step-response of the system. The coefficients are defined in order to obtain a fast response, so that the control scheme can compensate for fast disturbances of the pressure field. The coefficients identified, from an iterative procedure aimed to get the fastest response without the destabilisation of the system are $K_i = 2.3 \times 10^{15}\ V^2/s$, $K_p = 4.0 \times 10^{11}\ V^2$ and $K_d = 7.5 \times 10^5\ V^2 s$. It has to be noticed that the output of the PID controller can only be positive, so the control system is characterised by a zero-saturation. The design of the control system in this work has been done in order to reduce this at a minimum.

3.3 Flow Disturbance Rejection

The closed-loop aerodynamic response of the membrane wing previously considered is finally simulated under a external disturbance. The reference case considered is the

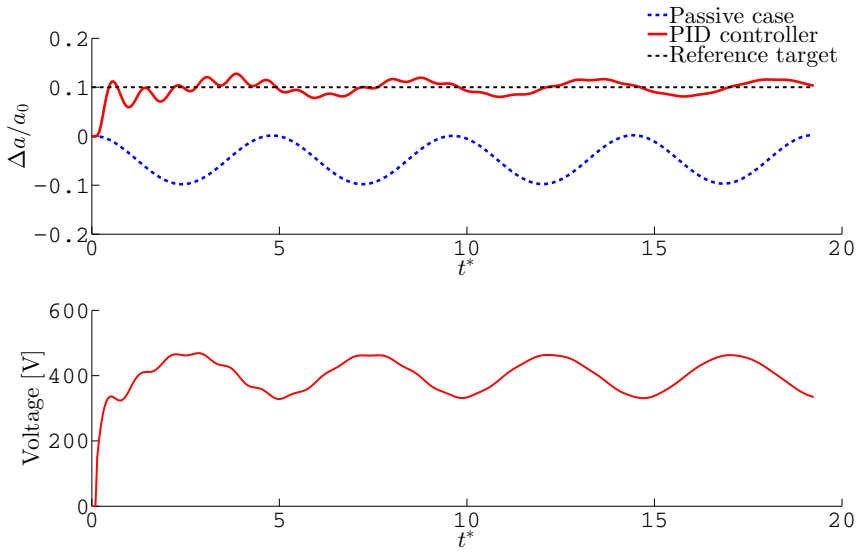

Figure 5: Comparison of the passive and feedback controlled cases for the case of the disturbance defined in (11). The target camber amplitude defined is 1.10 of the initial reference one. Results refer to the simulations in the high-fidelity model.

steady-state configuration for $\alpha = 4°$. The disturbance is simulated as a time-dependent variation of a constant pressure field directly applied on the walls of the wing, which is varied according to the harmonic law

$$\Delta P = P(1 - \cos(2\pi f_p t)), \tag{11}$$

where ΔP is variation in the pressure distribution. In this case P and f_p are set to 3% of the free stream dynamic pressure and 10 Hz respectively. Imposing directly the pressure variation on the wing allows to neglect the convective time scales of the fluid and precisely define the type of disturbance, in terms of amplitude and frequency, to which the wing is subjected to. Although it results in a non-physical problem, at this preliminary evaluation of the performance of a feedback control scheme on the wing, this assumption allows to target the problem and quickly identify the numerical issues related to the solution adopted.

Since the pressure is artificially applied to the system, an excellent system output into the control for this case is the membrane camber amplitude, a. This is also justified by the results in Fig. 3b, where the C_l behaviour is mainly determined by the first mode of the aeroelastic system, which is well approximated by the instantaneous membrane camber. As a result, considering the value of the lift coefficient or the maximum camber is essentially a matter of a scaling the coefficient in the controller designed in Sec. 2.4.

The wing response in the open- and closed-loop simulations is compared in Fig. 5. For the disturbance selected, the open-loop results show a reduction of 5% of the mean camber amplitude and oscillations of 5% around the reduced mean value. In the controlled case, the mean amplitude targeted is set to 1.1 of the initial reference value. It can be seen that the controller is bringing the value of the maximum camber amplitude close to the target one, with minimal oscillations as compared with the passive case. The actuation is not saturating because of the positive higher membrane amplitude considered as target.

4 Conclusions

This work has presented a high-fidelity computational framework and a subsequent procedure for controller design for actuated membrane wings. Numerical results have showed that the proposed model is capable of representing the system dynamics and therefore allows for the investigation of the structural and flow phenomena of the fully-coupled aeroelastic system, and the achievement of desired aerodynamic response using closed-loop strategies.

Numerical results have showed the potential for the feedback control of the wing for rejection of external disturbances. A system identification technique based on the Eigensystem Realization Algorithm has been used to define a low order description of the aeroelastic system to be used in the preliminary design of the PID-type control system. The designed controller has been applied to the high-fidelity model for the compensation of flow disturbances. On the one hand, this preliminary investigation has demonstrated the potential of embedded actuation for aerodynamic control in MAVs, but on the other hand, it has also highlighted the need for a more suitable control strategies that consider the constraints imposed by the zero-voltage saturation.

Results have also highlighted the advantages of the system identification methodology proposed in this work to allow a cheap iterative procedure for the control-system design, considering a large time window. The long term aerodynamic response of the wing in a closed loop response, and a preliminary energy balance of the controlled system will be the subject of the future work of the authors.

Acknowledgements

The authors acknowledge the financial support of the European Office of Aerospace Research & Development of the US Air Force Office of Scientific Research, and the UK Engineering and Physical Sciences Research Council Grant EP/J002070/1, "Towards Biologically-Inspired Active-Compliant-Wing Micro-Air-Vehicles".

References

[1] Y. Winter and O. Von Helversen. The energy cost of flight: Do small bats fly more cheaply than birds? *Journal of Comparative Physiology B*, 2:105–111, 1998.

[2] R. Albertani, B. Stanford, J. Hubner, and P. Ifju. Aerodynamic coefficients and deformation measurements on flexible micro air vehicle wings. *Experimental Mechanics*, 47:625–635, 2007.

[3] B.G. Newman. Aerodynamic theory for membranes and sails. *Progress in Aerospace Sciences*, 24:1–27, 1987.

[4] P. Rojratsirikul, Z. Wang, and I. Gursul. Unsteady fluid structure interactions of membrane airfolis at low reynolds numbers. *Experiments in Fluids*, 46:859–872, 2009.

[5] P. Rojratsirikul, Z. Wang, and I. Gursul. Flow-induced vibrations of low aspect ratio rectangular membrane wings. *Journal of Fluids and Structures*, 27:1296–1309, 2011.

[6] S. Arbos-Torrent, B. Ganapathisubramani, and R. Palacios. Leading- and trailing-edge effects on the aeromechanics of membrane aerofolis. *Journal of Fluids and Structures*, 38:107–126, 2013.

[7] Z. Suo. Theory of dielectric elastomers. *Acta Mechanica Solida Sinica*, 23:549–577, 2010.

[8] Harold S. Park, Qiming Wang, Xuanhe Zhao, and Patrick A. Klein. Electromechanical instability on dielectric polymer surface: Modeling and experiment. *Computer Methods in Applied Mechanics and Engineering*, 260:40–49, June 2013.

[9] R. Bleischwitz, R. de Kat, , and B. Ganapathisubramani. Aspect-ratio effects on aeromechanics of membrane wings at moderate Reynolds numbers. *AIAA Journal*, 53(3):780–788, March 2015.

[10] R. W. Smith and W. Shyy. Computational model of flexible membrane wings in steady laminar flow. *AIAA Journal*, 33:1769–1777, 1995.

[11] S. Tiomkin, D.E Raveh, and R. Arieli. Parametric study of a two-dimensional membranw wing in viscous laminar flow. In *29th AIAA Applied Aerodynamics Conference*, Honolulu, Hawaii, USA, June 2011.

[12] R. E. Gordnier. High fidelity computational simulation of a membrane wing airfoil. *Journal of Fluids and Structures*, 25:897–917, 2009.

[13] Y. Lian, W. Shyy, D. Viieru, and B. Zhang. Membrane wing aerodynamics for micro air vehicles. *Progress in Aerospace Sciences*, 39:425–465, 2003.

[14] Y. Lian and W. Shyy. Laminar-turbulent transition of a low Reynolds number rigid or flexible airfoil. *AIAA Journal*, 45:1501–1513, 2007.

[15] S. Buoso and R. Palacios. Electro-aeromechanical modelling and feedback control of actuated membrane wings. In *23nd AIAA/AHS Adaptive Structures Conference*, Kissimmee, Florida, USA, January 2015.

[16] M.R. Hays, J. Morton, B. Dickinson, U.K. Chakravarty, and Oates W.S. Aerodynamic control of micro air vehicle wings using electroactive membranes. *Journal of Intelligent Material Systems and Structures*, 24(7):862–878, May 2013.

[17] O.M. Curet, A. Carrere, R. Waldman, and K.S. Breuer. Aerodynamic characterisation of a wing membrane with variable compliance. *AIAA Journal*, 52:1749–1756, 2014.

[18] *SIMULIA ABAQUS FEA 6.13, User Documentation.* Dassault System, 2013.

[19] J. Bonet. Large strain viscoelastic constitutive models. *International Journal of Solids and Structures*, 38, 2001.

[20] J. Bonet and R.D. Wood. *Nonlinear continuum mechanics for finite element analysis.* Cambridge, UK: Cambridge University Press, 2008.

[21] J.C. Simo and T.J.R. Hughes. *Computational inelasticity.* Springer: Interdisciplinary applied mathematics: Mechanics and materials, 1998.

[22] A.N. Gent. A new constitutive relation for rubber. *Rubber Chemistry Technology*, 69, 1996.

[23] S. Buoso and R. Palacios. A nonlinear viscoelastic model for electroactive inflated membranes. In *11th World Congress on Computational Mechanics*, pages 4300–4312, Barcelona, July 2014.

[24] J. Fox and N. Goulbourne. On the dynamic electromechanical loading of dielectric elastomer membranes. *Journal of the Mechanics and Physics of Solids*, 56:2669–268, 2008.

[25] J. Fox and N. Goulbourne. Electric field-induced surface transformations and experimental dynamic characteristics of dielectric elastomer membranes. *Journal of the Mechanics and Physics of Solids*, 57:1417–1435, 2009.

[26] *User guide, STAR-CCM+ version 8.04.* CD-adapco, 2013.

[27] S.B. Pope. *Turbulent flows.* Cambridge University Press, New York, 1st edition, 2000.

[28] K. Valen-Sendstad, K.A. Mardal, M. Mortensen, B.A.P Reif, and H.P. Langtangen. Direct numerical simulation of transitional flow in a patient-specific intercranial aneurysm. *Journal of Biomechanics*, 44:2826–2832, 2011.

[29] J.N. Juang and M.Q. Phan. *Identification and control of mechanical systems.* Cambridge University Press, New York, 1st edition, 2001.